Vision-based magnetic actuator positioning for wireless control of microrobots

Azaddien Zarrouk, Karim Belharet, Omar Tahri

Version of Record: https://www.sciencedirect.com/science/article/pii/S0921889019303604
Manuscript_4ab7a581932a1b485626ca9bebbf88db

Vision-based magnetic actuator positioning for wireless control of microrobots

Azaddien Zarrouk[a], Karim Belharet[b], Omar Tahri[a]

[a] *INSA Centre Val de Loire, Université d'Orléans, PRISME EA 4229, Bourges, France*
[b] *HEI campus Centre, Université d'Orléans, PRISME EA 4229, Chteauroux, France*

Abstract

This work is concerned with targeted drug delivery inside the human body using magnetic microrobots. It proposes a vision-based magnetic platform for guiding microrobots in both open-loop/closed-loop schemes. The open-loop scheme can be used for example in the case of the inner ear, where the microrobots cannot be localized in real time. On the other hand, for more accuracy, closed-loop scheme can be used for organs as the human eye since microrobots can be localized using a vision sensor. For both schemes, the platform is designed to compensate for human body movements. It is composed of a new magnetic actuator mounted on a robot end-effector and a hybrid vision system. The latter consists of a camera and two microscopes, while the newly proposed magnetic actuator is built using four permanent magnets. The proposed actuator has been designed to create a local maximum of the magnetic field magnitude in a planar workspace. This results in a convergence point for magnetic microrobots that are in its influence zone, making possible open-loop control with a satisfactory accuracy. The procedures for calibrating each component of the proposed platform are described and validated. Finally, several experiments have been carried out to validate the modeling part and to show the feasibility of the concept. The obtained experimental results show that using such platform, the microrobots guiding can be achieved in open-loop under reasonable perturbations and in closed-loop with an accuracy of $200\mu m$.

*Corresponding author
Email addresses: azaddien.zarrouk@insa-cvl.fr (Azaddien Zarrouk), karim.belharet@yncrea.fr (Karim Belharet), omar.tahri@insa-cvl.fr (Omar Tahri)

1. INTRODUCTION

Manipulation of objects using an external magnetic field inside human body is a strong challenge in the drug delivery applications. Therapeutic and diagnostic possibilities offered by such technology are growing with the clinical need to make procedures less invasive for the patients. There are many previous works discussing manipulations of magnetic particles using an external magnetic field for medical use. Ophthalmologists were the first to explore manipulation of magnetic objects in 1842. The first step in intravascular magnetic guiding was accomplished in the early 1950 [1]. The use of magnetic catheters to remove a foreign body in the stomach appeared in the 1940s [2] [3]. More recently, magnetic propulsion of capsule endoscopy has been also under investigation [4, 5, 6]. Magnetic guidance was also used in neurosurgery, especially for steering of magnetic catheters into cerebral vessels [7].

For all applications mentioned above a magnetic field is used to produce force or torques on a magnetic object located inside organ of the human body. To make a magnetic object reach its desired location, the external magnetic field has to be shaped by an accurate control currents or/and positioning of electromagnets or permanent magnets. The magnetic field of an electromagnet is produced by an electric current unlike the permanent magnets that need no power and no cooling device. This makes it possible to design a portable and light magnetic actuator based permanent magnets, which can mounted on the end-effector of robotic manipulator. However, in practice it is much more challenging to design a permanent-magnet based actuator with a well defined and accurate shape of the magnetic field. As related work, Mahoney et al [8] developed a control of a magnetic capsule endoscope, navigating in fluid by using a single permanent magnet coupled to a robotic manipulator. In [9], the same authors demonstrated the ability to control an untethered magnetic microrobot using a single rotating permanent magnet. In [10, 11, 12], a large magnet was displaced and oriented either manually or using a robotic platform to guide different versions of capsule endoscopy. A comparison between robotic versus manual magnetic steering is proposed by the same authors [13]. In the clinical field, the wireless Stereotaxis Niobe magnetic navigation system uses two permanent magnets to guide magnetically tips catheters in

the cardiovascular system [14]. The majority of magnetic actuators existing to date are based on closed-loop control for precise motion in the presence of perturbations generated by thermal noise or drifting due to boundary effects. It means that a localization system to recover the position of the microrobot is required. The localization system is very often a vision system, which is not always possible in a closed environment like a human body.In this paper, we propose a magnetic platform, capable of controlling a magnetic microrobot in both an open loop or closed-loop schemes. The first contribution of this work is a four permanent magnet based actuator capable of wireless position control of an untethered microrobot in 2D workspace even in the presence of reasonable perturbations. Its particularity is the creation of local maximum of magnetic field magnitude at a distance that acts as a point of convergence, and allows open-loop control of the magnetic microrobots. The second contribution is the calibration method of a hybrid vision system composed of a camera and two microscopes. This system creates a link between micro scale environment where the microrobots are guided and the macro scale where the magnetic actuator is controlled. There are some techniques in the literature dealing with the calibration of non-overlapping cameras. For example, in [15], the authors estimate the relative pose between two rigidly linked cameras using estimated motion between two different positions and more. In [16], a mirror is used to overcome the non-overlapping fields of view. The solutions proposed in [15, 16] cannot be applied to our system. First, because our platform is fixed, then the microscopes and the camera are observing objects with different scale. Therefore, using the motion of the vision system or a mirror to observe a calibration pattern by the camera and the microscopes at the same time is not feasible.

The remaining of this paper is organized as follows: the next Section explains the principle and modeling of the proposed actuator. In Section 3, a method for calibrating the hybrid vision system composed of a camera and two microscopes is provided. Then, Section 4 shows the experimental results using the proposed platform. The paper is concluded in Section 5.

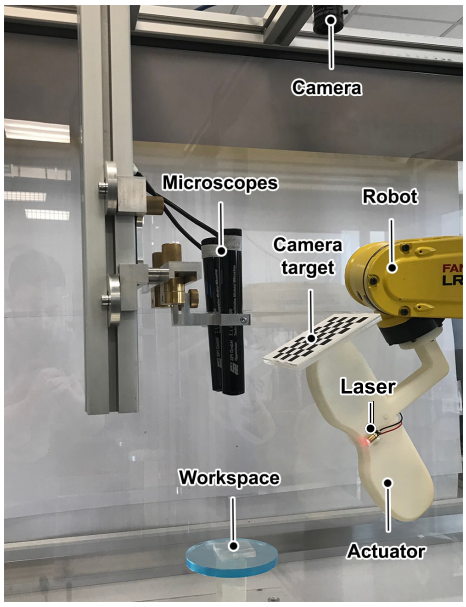

Figure 1: Experimental setup shows the different components of the platform.

2. Four permanent magnet based actuator

In the following of this section, it will be shown that with a combination of four permanent magnets a local maximum of the magnetic field can be created at some distance. The obtained local maximum will define a local convergence point inside its influence zone thanks to the produced attractive force by magnetic field gradient.

The magnetic field vectors and their magnitude generated by a system of two permanent magnets in xz-plane at $y = 0$ are shown in Fig. 2 (a). If the magnetization of the magnets is inverted, the magnetic field vectors change the direction while keeping the same magnitude. The resulting magnetic field combining two permanent magnet systems is the sum of the magnetic fields generated by each the two systems. From this, an idea to maximize locally the magnetic field strength becomes possible if we superimpose the two systems together (Fig. 2 (c) and (d)), in such way the magnets of the second system do not touch physically the magnets of the first system. At the same time, keep their magnetic field strength close to magnetic field strength of the first system to avoid the difference in field strength between the two systems.The magnetic

field generated by one rectangular permanent magnet (**i**) at point $\mathbf{x} = [x, y, z]^T$ as given by [17] is a function of the following parameters:

$$\mathbf{B_i}(\mathbf{x}) = f(\mathbf{x}, \mathbf{p}, \omega, \mathbf{M_{mag}}) \tag{1}$$

where $\mathbf{p} = [p_x, p_y, p_z]^T$ and $\omega = [\theta, \phi, \psi]^T$ are the position and the orientation vectors of the magnet, and $\mathbf{M_{mag}}$ is the magnetization of the magnet.

The additive property of magnetic field gives the following equation:

$$\mathbf{B_{total}} = \mathbf{B_{sys1}} + \mathbf{B_{sys2}} \tag{2}$$

where $\mathbf{B_{total}}$ is the resulting magnetic field of the two systems, $\mathbf{B_{sys1}} = \mathbf{B_{mag1}} + \mathbf{B_{mag2}}$ is the magnetic field of the two magnets of system 1 and $\mathbf{B_{sys2}} = \mathbf{B_{mag3}} + \mathbf{B_{mag4}}$ is the magnetic field of the two magnets of the system 2. As the force is directed from region of low to high magnetic field strength, we will focus on the magnetic field strength to have an idea about the resulting magnetic force directions. From equation (2), we can write:

$$\left\|\mathbf{B_{total}}\right\|^2 = \left\|\mathbf{B_{sys1}}\right\|^2 + \left\|\mathbf{B_{sys2}}\right\|^2 + 2\left\|\mathbf{B_{sys1}}\right\| \cdot \left\|\mathbf{B_{sys2}}\right\| cos(\Theta)$$

where Θ is the angle between the magnetic field of the two systems at point (x, y, z) in space projected in xz-plane at y=0 (see Fig. 3). From the equation (3), we see clearly that the magnetic field strength at point (x, y, z) in space is maximum when the angle $\Theta = 0$, and minimum when $\Theta = \pi$. In our case the magnitude of magnetic field generated by the two systems is of the same order, so the angle varies clearly the magnitude of the resulting magnetic field. We obtain the local maximum by fixing the magnets of the system 1, then varying the position and the orientation of the magnets of system 2 while keeping symmetry with respect to **y**-axis.

The generation of local maximum is shown in Fig. 3, where the magnetic field strength at each point is given by vector magnitude. It is clear that moving away from point $[0, 0, 5.93]^T \times cm$ in this case, the angle Θ between the magnetic field vectors of system 1 and system 2 varies from 0 until reaching the maximum value of π. Consequently, the magnitude of the resulting vectors decreases in turn. We are interested in the area above $z = 5.93 \times cm$, because we know that when moving away from the

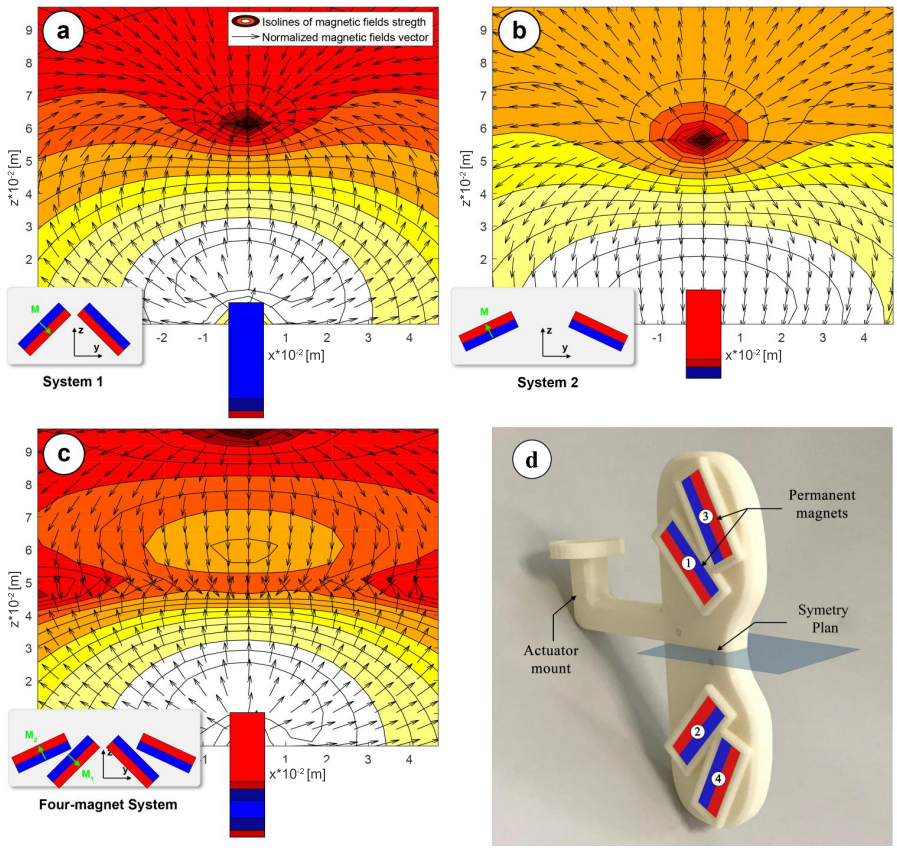

Figure 2: (a) Magnetic field strength and direction of system 1: the heat map represents the magnetic field strength generated by the magnetic system composed of two permanent magnets, positioned as shown in the small scheme at the bottom left. The black vectors represent the normalized magnetic field direction, and the green vector in the small scheme gives the magnetization direction of the magnets. (b) Magnetic field strength and direction of system 2. The difference from the system in (a) is the magnetization direction of the magnets. Magnets in (a) and magnets in (b) have a magnetization in opposite directions. c) and d): Novel four-magnet based actuator superimposing both configurations (a) and (b).

magnets, the magnetic field decreases naturally whatever the configuration of the four magnets. Below $z = 5.5 \times cm$, the angle Θ is close to π which minimizes locally the magnetic fields. Fig. 4 shows the magnetic force direction and strength in the area around the convergence point. The trajectory of microrobots placed in different initial positions is shown in this area to demonstrate that without any control efforts, the microrobots converged to a known position, which is the actuator convergence point.

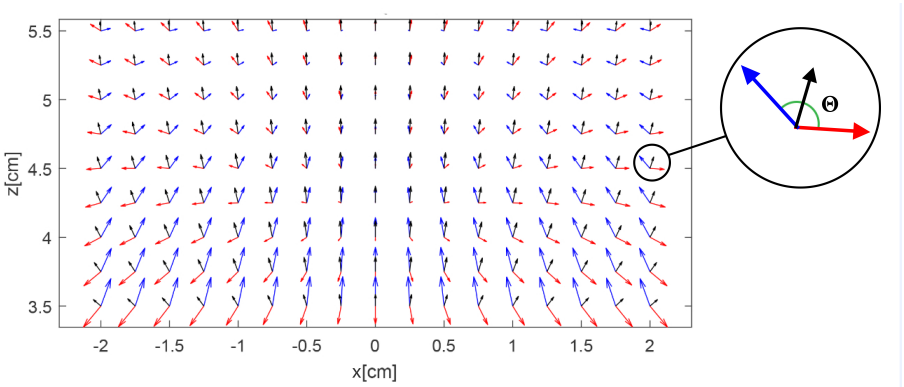

Figure 3: Magnetic field vectors in xz-plane of each system (red vector for system 1 and blue vectors for system 2) and resulting magnetic field of the two systems around the created local maximum in xz-plane.

When mounting the system on robot manipulator end-effector or any XYZ positioning stage, the stabilization point can be placed at any desired position using simply translational motions. It ensures open-loop control of the microrobot when evolving in confined environments where visual sensors are useless. Besides, if the organ is accessible and the microrobot position can be measured in real time using vision sensors, visual servoing can be used in such case for more accurate control.

3. Hybrid vision system

3.1. Calibration challenges and notations

The vision system is composed of a camera and stereo system of two microscopes. It has been proposed to meet several needs in the proposed platform, including the need to validate the model of microrobots inside viscous environment, to validate the actuator magnetic model in order to obtain the best performance in the open-loop scheme and finally to control microrobots in closed-loop when they can be localized in real time. In order to use the proposed system, it is necessary to calibrate its different components. Calibrating the hybrid vision system (Fig.5) consists in estimating the intrinsic parameters of each sensor and the relative poses of the two microscopes with respect to the camera. This has to overpass two challenges. The first is the scale difference

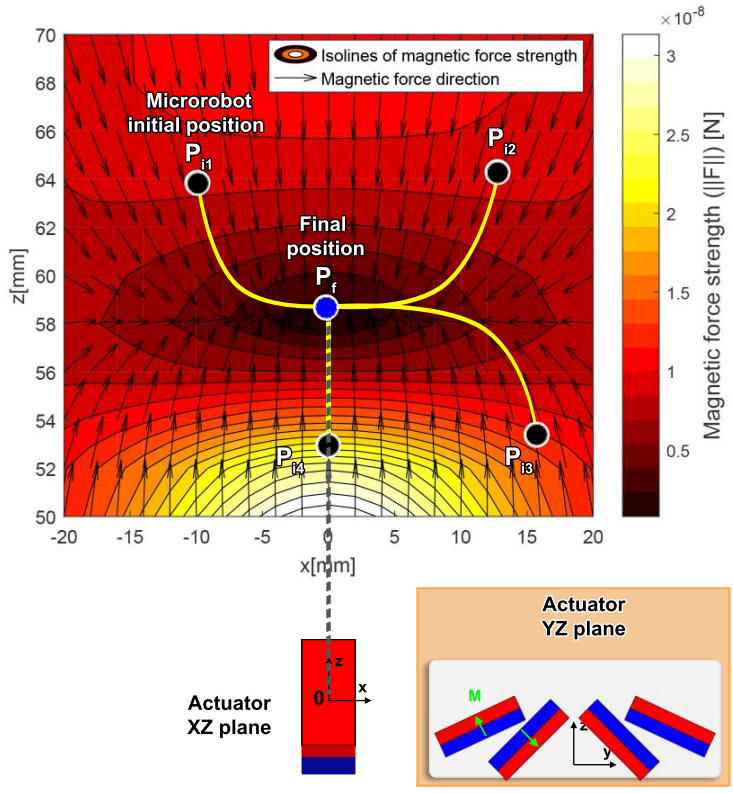

Figure 4: The four-magnet system and the area around its convergence point in xz-plane. Black dots are microrobots in different positions, and yellow narrows are the trajectories released by the microrobots because of the effect of the convergence point. The scheme at the bottom-right corner represents the actuator design in the yz-plane.

between the camera and the microscopes. The second is the non-overlapping fields of the sensors. In the following, our proposed calibration method is explained.

The following notations are adopted for the different parameters to be estimated:

- $\mathbf{K}_{cam}$, $\mathbf{K}_{mic1}$ and $\mathbf{K}_{mic2}$ are respectively the matrices of the intrinsic parameters of the camera and those of the two microscopes.
- ${}^{cam}\mathbf{T}_{mic1}$, ${}^{cam}\mathbf{T}_{mic2}$ and ${}^{mic1}\mathbf{T}_{mic2}$ are respectively the homogeneous transformations between microscope 1 and camera, microscope 2 and camera, and microscope 2 and microscope 1.

Recall that the matrix of the intrinsic parameters $\mathbf{K}$ is defined by:

$$\mathbf{K} = \begin{bmatrix} \alpha & 0 & u_0 \\ 0 & \beta & v_0 \\ 0 & 0 & 1 \end{bmatrix} \tag{3}$$

where α and β are the scale factors of the image, u_0 and v_0 are the coordinates of the optical center of the camera in the image frame.

The homogeneous transformation ${}^{\mathbf{b}}\mathbf{T}_{\mathbf{a}}$ is defined from rotation matrix ${}^{\mathbf{b}}\mathbf{R}_{\mathbf{a}}$ and translation vector ${}^{\mathbf{b}}\mathbf{t}_{\mathbf{a}}$ as follows:

$${}^{\mathbf{b}}\mathbf{T}_{\mathbf{a}} = \begin{bmatrix} {}^{\mathbf{b}}\mathbf{R}_{\mathbf{a}} & {}^{\mathbf{b}}\mathbf{t}_{\mathbf{a}} \\ 0 & 1 \end{bmatrix} \tag{4}$$

3.2. Calibration method

The main problem in calibrating the hybrid vision system is to estimate the homogeneous transformation ${}^{cam}\mathbf{T}_{mic1}$ and ${}^{cam}\mathbf{T}_{mic2}$, between the camera and the microscopes. To calibrate such vision system, firstly, the camera and the microscopes are calibrated separately in order to obtain their intrinsic parameters. Secondly, we created a rigid link between the microscopes and camera field of view using two patterns rigidly linked as shown in Fig. 6.

The calibration process is as follows: firstly, the calibration pattern is positioned such that the microscopes are able to observe the small grid and the big grid is visible

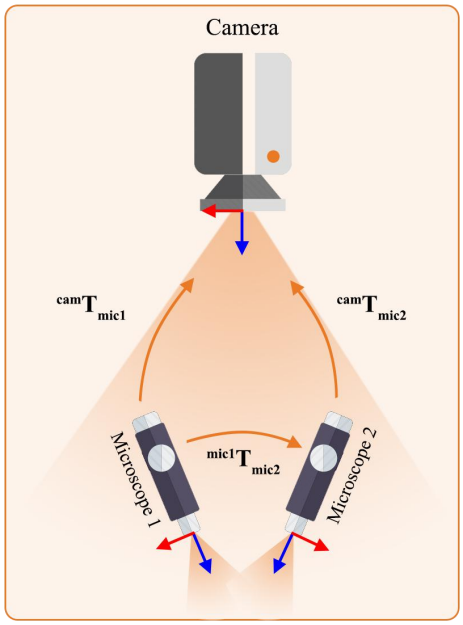

Figure 5: The hybrid vision system with the various unknown homogeneous transformations between sensors coordinate systems.

for the camera. For each position of the calibration pattern, images are acquired by each sensor. Then, using a conventional calibration procedure for each acquired image, the corresponding pose of the big grid with respect to the camera ${}^{cam}\mathbf{T}_M$ can be recovered. The poses ${}^{mic1}\mathbf{T}_m$ and ${}^{mic2}\mathbf{T}_m$ of the small grid with respect to the microscopes can be estimated in the same way.

The last step uses the fact that the homogeneous transformation ${}^{M}\mathbf{T}_m$ between the two planar patterns is fixed and known to obtain the unknown relative pose between the camera and the two microscopes.

For the relative pose between the camera and microscope 1, decomposing ${}^{cam}\mathbf{T}_{mic1}$ gives:

$$ {}^{cam}\mathbf{T}_{mic1} = {}^{cam}\mathbf{T}_M \, {}^{M}\mathbf{T}_m \, {}^{m}\mathbf{T}_{mic1} \tag{5} $$

Equation (5) can be rewritten as follows:

$$ {}^{cam}\mathbf{T}_{mic1} = {}^{cam}\mathbf{T}_M \, {}^{M}\mathbf{T}_m \, {}^{mic1}\mathbf{T}_m^{-1} \tag{6} $$

Likewise, the homogeneous transformation between camera and microscope 2 coordinate systems can be written as follows:

$$^{cam}\mathbf{T}_{mic2} = {}^{cam}\mathbf{T}_{M}\,{}^{M}\mathbf{T}_{m}\,{}^{mic2}\mathbf{T}_{m}{}^{-1} \tag{7}$$

Using equations (6) and (7), the homogeneous transformation between the camera and each microscope can be obtained from a single position of the calibration pattern. However, for robustness purpose, more than one pattern positions should be used.

3.3. Calibration refinement using bundle adjustment

In this part, a procedure to refine the hybrid system parameters using bundle is proposed. For that, it is necessary to define a cost function taking into account reprojection errors in the camera image plane and microscopes image plane as well. Actually, reprojection errors are defined from the difference between extracted points in the image plane and those computed based on the vision sensor model and pattern/sensor pose. In our case, it is necessary to define a cost function considering the microscopes/camera pose in the minimization process, while using a minimal number of parameters. To respect these conditions, we defined three cost functions as follows:

- For the camera:

$$e_{cam} = \sum_{i=1}^{n}\sum_{j=1}^{m_c} \left\| \mathbf{x}_{c_{ij}} - f_1(\mathbf{K}_{cam}, {}^{cam}\mathbf{T}_{M_i}, \mathbf{X}_{M_j}) \right\|^2 \tag{8}$$

- For the microscope 1:

$$e_{mic1} = \sum_{i=1}^{n}\sum_{j=1}^{m_m} \left\| \mathbf{x}_{m1_{ij}} - f_2(\mathbf{K}_{mic1}, {}^{mic1}\mathbf{T}_{cam}, {}^{cam}\mathbf{T}_{M_i}, \mathbf{X}_{m_j}) \right\|^2 \tag{9}$$

- For the microscope 2:

$$e_{mic2} = \sum_{i=1}^{n}\sum_{j=1}^{m_m} \left\| \mathbf{x}_{m2_{ij}} - f_3(\mathbf{K}_{mic2}, {}^{mic2}\mathbf{T}_{cam}, {}^{cam}\mathbf{T}_{M_i}, \mathbf{X}_{m_j}) \right\|^2 \tag{10}$$

where:

- n is the number of the acquired images, m_c is the number of points extracted from the image acquired by the camera, while m_m is the number of those extracted from the microscope image.
- $\mathbf{X_{M_j}} = [x_{c_j}, y_{c_j}, 0]^T$ is coordinate vector of point j in the big grid coordinate system.
- $\mathbf{X_{m_j}} = [x_j, y_j, 0]^T$ is coordinate vector of point j in the big grid coordinate system.
- $\mathbf{x}_{c_{ij}} = [u_{c_{ij}}, v_{c_{ij}}]^T$ and f_1 are respectively the coordinate of measured point j of image i and the projection of point $\mathbf{X_{wc_j}}$ in image i acquired by the camera
- $\mathbf{x}_{m1_{ij}} = [u_{m1_{ij}}, v_{m1_{ij}}]^T$, $\mathbf{x}_{m2_{ij}} = [u_{m2_{ij}}, v_{m2_{ij}}]^T$, f_2 and f_3 are respectively the coordinate of measured point j of image i and the projections of point $\mathbf{X_{w_j}}$ in image i acquired by the first and second microscope. Note that differently from f_1, the homogeneous transformations used in the reprojection f_2 and f_3 were decomposed to include the homogeneous transformation camera/microscopes.

The equation (8) minimizes the reprojection error in the image plane of the camera by optimizing its intrinsic and extrinsic parameters. The equations (9) and (10) will minimize the reprojection error in the microscope 1 and microscope 2 respectively by optimizing their intrinsic parameters and relative poses with respect to the camera. The global cost function is defined as the sum of the three previous ones:

$$e = e_{cam} + e_{mic1} + e_{mic2} \tag{11}$$

Finally, Levenberg-Marquardt algorithm [18] is used to solve the nonlinear minimization problem of the cost function e.

4. Vision based actuator positioning and microrobot steering

This section explains the full process for magnetic microrobot steering by accurately positioning the four-magnet actuator with respect to the micro-workspace using the hybrid vision system. This includes the microrobot trajectory planning in the micro-workspace and the necessary trajectory to be followed by the robot end-effector to position adequately the four-magnet actuator.

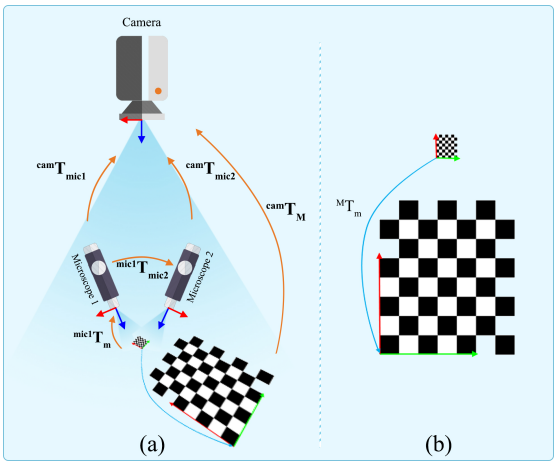

Figure 6: Calibration of the hybrid vision system using planar patterns of two different scales: a) transformation decomposition, b) the planar patterns separated by pure translational motions.

4.1. Vision-based actuator positioning and microrobot steering strategy

The full process is shown on Fig.9. First, the trajectory to be followed by the microrobot in the micro-scale workspace is defined and discretized into m intermediate goal positions ${}^{m}\mathbf{x}_d = [x_d, y_d, 0]^T$.

The coordinates of the points ${}^{m}\mathbf{x_d}$ are then expressed in the end-effector frame and noted ${}^{eff}\mathbf{x_d}$ by:

$$ {}^{eff}\mathbf{x}_d = {}^{eff}\mathbf{T}_m \, {}^{m}\mathbf{x}_d \tag{12} $$

The homogeneous transformation ${}^{eff}\mathbf{T}_m$ can be decomposed as follows:

$$ {}^{eff}\mathbf{T}_m = {}^{eff}\mathbf{T}_{target} \, {}^{target}\mathbf{T}_{cam} \, {}^{cam}\mathbf{T}_{mic} \, {}^{mic}\mathbf{T}_m \tag{13} $$

where as shown in Fig.7:

- ${}^{mic}\mathbf{T}_m$: the relative pose of the micro-workspace with respect to the microscopes frame. This later is defined with the aid of markers seen detected with microscopes.
- ${}^{eff}\mathbf{T}_{target}$: the relative pose of the target frame with respect to the robot end-effector frame. This rigid pose obtained after robot-camera calibration which a classical problem in robotics field that have been sufficiently studied [19, 20].

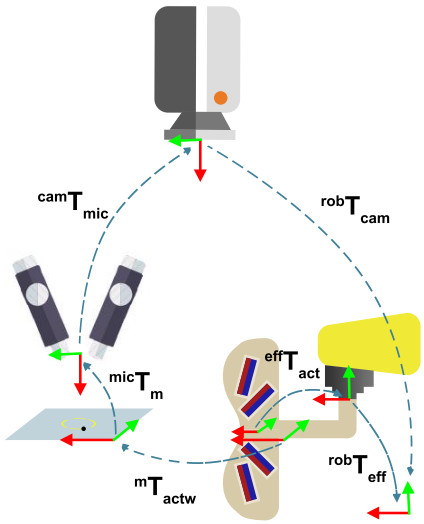

Figure 7: Different relative poses between the vision based platform components.

- ${}^{target}\mathbf{T}_{cam}$: the relative pose of the camera with respect to the target obtained thanks to the known structure of the grid.
- ${}^{cam}\mathbf{T}_{mic}$: the relative pose of the microscopes frame with respect to the camera, obtained thanks to the proposed calibration method of the hybrid vision system.

Since the convergence point has rigid position with respect to the robot end-effector, the microrobot trajectory is expressed at the end-effector because the desired trajectory will be realized by the convergence point, thus by the robot end-effector (see Fig.8). The motion to be applied to the robot end-effector is defined by the translation between the convergence point expressed in the end-effector frame and a desired point expressed in the same frame. The convergence point position with respect to the effector may be obtained using the actuator 3D model. In the experimental platform, errors may come from the 3D printing of the actuator and when mounting the actuator on the effector. A calibration step has been performed to avoid these errors thanks to the calibrated hybrid vision system. The calibration step was performed as follows: the actuator mounted on robot manipulator has been driven to position the convergence point in the workspace under the microscopes where a microrobot is placed. As the microrobot converges to

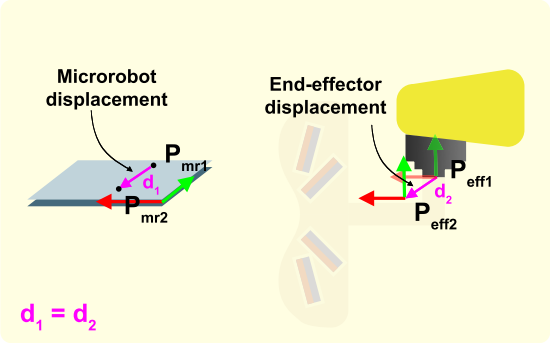

Figure 8: robot-end effector displacement when moving microrobot from position to another.

this point, its position can be recovered thanks to the microscopic stereo system. Let ${}^{mic}\mathbf{x}_{cp}$ be the position of the convergence point under the microscopic stereo system. This position is transformed into the robot end-effector using the camera. In fact, the camera creates a link between the frame of the robot and that of the microscopes thanks to the already calibrated hybrid vision system and the robot-camera calibration step. The last calibration problem is a classical problem in robotics field that have been sufficiently studied [19, 20]. Thus, the convergence point position with respect to the end-effector ${}^{eff}\mathbf{x}_{cp}$ is obtained with the following equation:

$$ {}^{eff}\mathbf{x}_{cp} = {}^{eff}\mathbf{T}_{target}\,{}^{target}\mathbf{T}_{cam}\,{}^{cam}\mathbf{T}_{mic}\,{}^{m}\mathbf{x}_{cp} \tag{14} $$

Once the calibration step is done, the translation motion from the actual convergence point position to a desired position is then calculated as follows:

$$ {}^{eff}\mathbf{t}_{\mathbf{i}eff2} = {}^{eff}\,\mathbf{x_{id}} - {}^{eff}\,\mathbf{x_{cp}} \tag{15} $$

The calculated translation is given to the robot to move the end-effector from a desired point to another. As the end-effector moves, the other desired points position has to be updated with respect to the new end-effector frame.

The proposed strategy allows two vision-based tracking possibilities. As seen on Fig.9 camera can be selected to track markers on the workspace. In this case ${}^{mic}\mathbf{T}_{m}$ is calculated as follows:

$$ {}^{mic}\mathbf{T}_{m} = {}^{mic}\mathbf{T}_{cam}\,{}^{cam}\mathbf{T}_{M}\,{}^{M}\mathbf{T}_{m} \tag{16} $$

where ${}^{cam}\mathbf{T}_M$ is the pose of the markers in the camera frame, and ${}^{M}\mathbf{T}_m$ is the relative pose of the micro-workspace frame with respect to the markers.

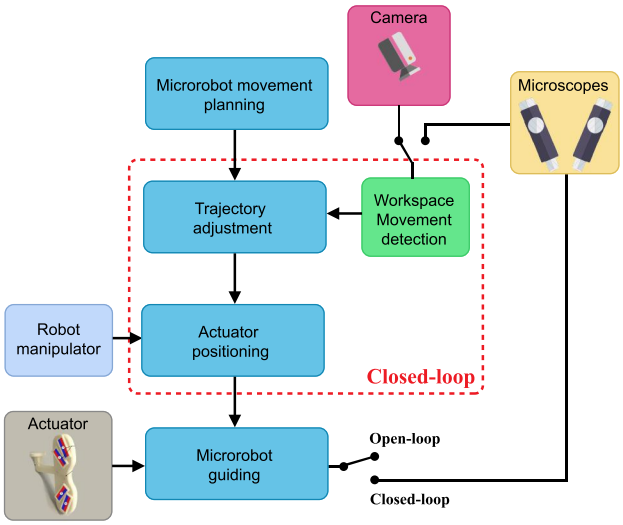

Figure 9: Microrobot steering strategy using the hybrid vision system and the four-magnet actuator.

From equation (14), one can see that positioning the actuator with respect to the workspace is ensured in real time with the calibrated hybrid vision system. However, once the planned trajectory is defined, the positioning is achieved in open-loop with no feedback on the microrobot location. Therefore, the hybrid vision system serves only for positioning the actuator in the workspace. This feature is important in medical field to take into account the movements of the patient during the treatment. For example to guide microrobots inside the inner ear (cochlea), the trajectory is planned initially to be released in open-loop. However, once the patient's head moves, the planned trajectory should be corrected with respect to the new position of the head. On the other hand, the platform can track and correct the microrobot position when it is accessible for visual sensors (see Fig.9), like the case of the eye treatment. In this case, the microrobot position is estimated with the microscopes, the actual position is compared to the desired position and corrected to minimize the error.

4.2. Dynamic modeling of magnetic microrobot in viscous environment

The open-loop navigation of a magnetic microrobot is based on its dynamic model. This model allows to predict the time required for a microrobot to move from a point of the planned trajectory to the next one. In our context, the magnetic microrobot is in a viscous environment and subject to several types of forces: magnetic force, the viscous drag force of Stokes, inertia, buoyancy and gravity, thermal kinetics (Brownian motion), double-layer electrical interactions, and van der Waals force. Among those forces, the magnetic and the viscous ones are the most significant, while the others can be neglected [21, 22, 23].

Using second Newtons law, the microrobot dynamical model can be written as follows:

$$m_p \frac{\mathrm{d}\mathbf{v}_p}{\mathrm{d}t} = \mathbf{F_{mag}} + \mathbf{F_d} \tag{17}$$

where m_p and $\mathbf{v}_p$ are the mass and the velocity of the microrobot. $\mathbf{F_{mag}}$ and $\mathbf{F_d}$ are the magnetic force and the drag force respectively. The magnetic force on a spherical microrobot depends on the magnetic field gradient created at its position [24]:

$$\mathbf{F_{mag}} = V_m \left\| M \right\| .(\nabla \left\| \mathbf{B} \right\|) \tag{18}$$

where V_m is the volume of the magnetized object, $\mathbf{B}$ is the flux density of the applied magnetic field, and $\mathbf{M}$ is the magnetization of the microrobot. On the other hand, the magnitude of the fluidic force acting on a moving microrobot is determined by Stokes law:

$$\mathbf{F_d} = -6\pi\eta r \mathbf{v_p} \tag{19}$$

where η is the viscosity of the fluid, r is the radius of the microrobot, and $\mathbf{v}_\mathrm{p}$ is the velocity of the microrobot. Finally, the movement of a spherical microrobot immersed in a fluid and actuated by an external magnetic field, can be described by a system of ordinary differential equations (ODE):

$$\begin{cases} \dot{\mathbf{x}} = \mathbf{v_p} \\ \ddot{\mathbf{x}} = \frac{V_m}{m_p} \left\| M \right\| .(\nabla \left\| \mathbf{B} \right\|) - \frac{6\pi\eta r}{m_p} \dot{\mathbf{x}} \end{cases} \tag{20}$$

Using (20), it is possible to estimate the time necessary for a microrobot to reach a desired position.

5. Experimental validation

In the following of this section, first, the calibration results of the hybrid system are shown and discussed. Then the convergence point is experimentally proven and its coordinates in the end-effector frame estimated using the hybrid vision system. Finally, experimental results of microrobot steering in open-loop and closed-loop are shown.

5.1. Calibration of the hybrid vision system

First, the camera and the microscopic stereo system are calibrated separately and then their relative poses defined by ${}^{\text{cam}}\text{T}_{\text{mic1}}$ and ${}^{\text{cam}}\text{T}_{\text{mic2}}$ are obtained using equations (6) and (7). To further refine these results, the bundle adjustment technique is used to reformulate the optimization problem and Levenberg-Marquardt algorithm is used to solve it. The calibration results are evaluated in two different ways. Firstly, using reprojection errors in the image. Then, by testing the ability of the camera to control the position of a Laser beam mounted on a robot end-effector to target points observed by microscopes.

5.1.1. Calibration results before and after refinement

In the following, the extracted points from acquiring images by the two microscopes are compared to those calculated using following reprojection equations:

$$\mathbf{x}_{m1} = f_1(\mathbf{K}_{mic1}, {}^{mic1}\mathbf{T}_{cam}\,{}^{cam}\mathbf{T}_{M}\,{}^{M}\mathbf{T}_{m}, \mathbf{X}_w) \tag{21}$$

$$\mathbf{x}_{m2} = f_2(\mathbf{K}_{mic2}, {}^{mic2}\mathbf{T}_{cam}\,{}^{cam}\mathbf{T}_{M}\,{}^{m}\mathbf{T}_{m}, \mathbf{X}_w) \tag{22}$$

where $\mathbf{x}_{m1}$ and $\mathbf{x}_{m2}$ are the coordinates of the projected point in the two microscopes image plane and $\mathbf{X}_w$ is coordinate vector of point in world coordinate system. The transformations ${}^{\text{cam}}\mathbf{T}_{\text{mic1}}$ and ${}^{\text{cam}}\mathbf{T}_{\text{mic2}}$ have been introduced in the reprojection on images in order to test their accuracy.

For each microscope, the average and the standard deviation of the reprojection errors defined by equations (21) and (22) have been computed using 20 acquired images with 42 points each. The obtained results are shown in Table 5.1.1. The left column

shows the result obtained using equations (6) and (7) to estimate ${}^{cam}\mathbf{T}_{mic1}$ and ${}^{cam}\mathbf{T}_{mic2}$ before refinement. The average reprojection error and the standard deviation in image plane are around 12pixels and 7pixels respectively, which correspond to 634μm and 371μm in the small grid coordinate system. These results may appear huge at first sight but can be explained by the scale difference between the camera and the microscopes. Actually, small errors in the estimated camera poses could correspond to several pixels in the microscope image. Besides, the obtained results can be refined using a global optimization as explained in section 3. The results obtained after refinement are shown in the right column of Table. Compared to the initial results, the average projection error in the image plane is reduced by 92% and 90% for microscope 1 and microscope 2 respectively. In the small grid coordinate system, this error is reduced by 93% for microscope 1 and 91% for microscope 2.

Table 1: Calibration results of the hybrid vision system sensors before and after optimization.

	Microscope 1 Before|**After** bundle adjustment	Microscope 2 Before|**After** bundle adjustment
Average reprojection error (pixel)	13.78|**0.94**	11.72|**0.98**
Average standard deviation (pixel)	7.04|**0.50**	8.04|**0.49**
Average reprojection error (μm)	689.0|**47.0**	579.3|**48.6**
Average standard deviation (μm)	360.3|**25.7**	382.1|**24.2**

5.1.2. Validation of calibration method using a Laser beam

In this part, calibration results, accuracy is evaluated by testing the ability of the camera to point a Laser beam mounted on robot end-effector toward targets observed by the microscopes. The experimental setup is descried on Fig.10. It is composed of the

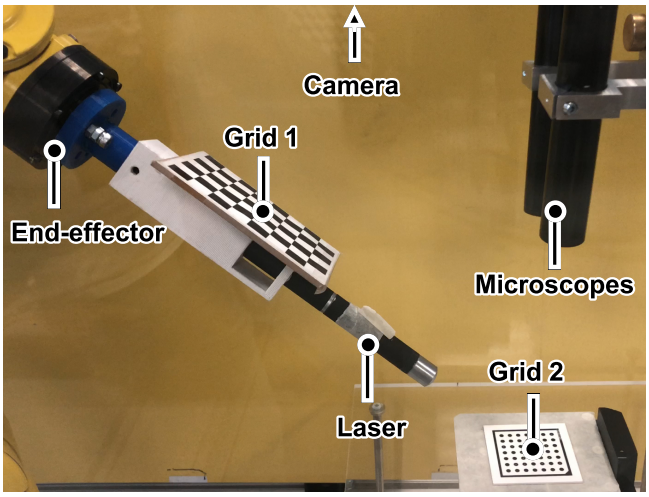

Figure 10: The proposed platform with Laser mounted on the robot manipulator instead of the magnetic actuator to validate the calibration method.

hybrid vision sensor, a Laser line beam mounted on the robot end-effector. The process for obtaining the rigid transformations 'Grid 1'/Laser and 'Grid 1'/robot are omitted on purpose and they are assumed to be known. Currently, the goal is to position the Laser beam toward points on the Grid 2 situated on the field of view of the microscopes. The Laser beam position is controlled using the pose of the grid (refer to Fig.10) in the camera frame. On the other hand, the 3D coordinates of the points of the Grid 2 (Fig.10) to be targeted by the Laser are expressed first in microscopes frame and then in the camera frame through the transformation ${}^{mic}T_{cam}$. In practice, there exists an infinity of the Laser motion to reach the points under the microscopes. In this experiment, to move the Laser from a position to another, pure translation and pure rotational motions of the robot end-effector has been used. To move from initially targeted point to target another point, the translation vector, rotation angle and axis are calculated using equations (23), (24) and (25).

$$\mathbf{t} = \mathbf{p_f} - \mathbf{p_0} \tag{23}$$

$$\mathbf{a} = \mathbf{p_i} \times \mathbf{p_1} \tag{24}$$

$$\theta = acos(\mathbf{p_i} \cdot \mathbf{p_1}) \tag{25}$$

As described in Fig 11, $\mathbf{t}$ is the translation vector to move from $\mathbf{p_0}$ to $\mathbf{p_1}$; $\mathbf{a}$ and θ are respectively the axis and the angle of rotation to move from $\mathbf{p_0}$ to $\mathbf{p_1}$; $\mathbf{p_f}$ is the projection of point $\mathbf{p_0}$ on the Laser line containing the point $\mathbf{p_1}$ (Fig 11a); $\mathbf{p_i}$ is the point belong to Laser line containing point $\mathbf{p_0}$ and have the same magnitude of point $\mathbf{p_1}$ (Fig 11b).

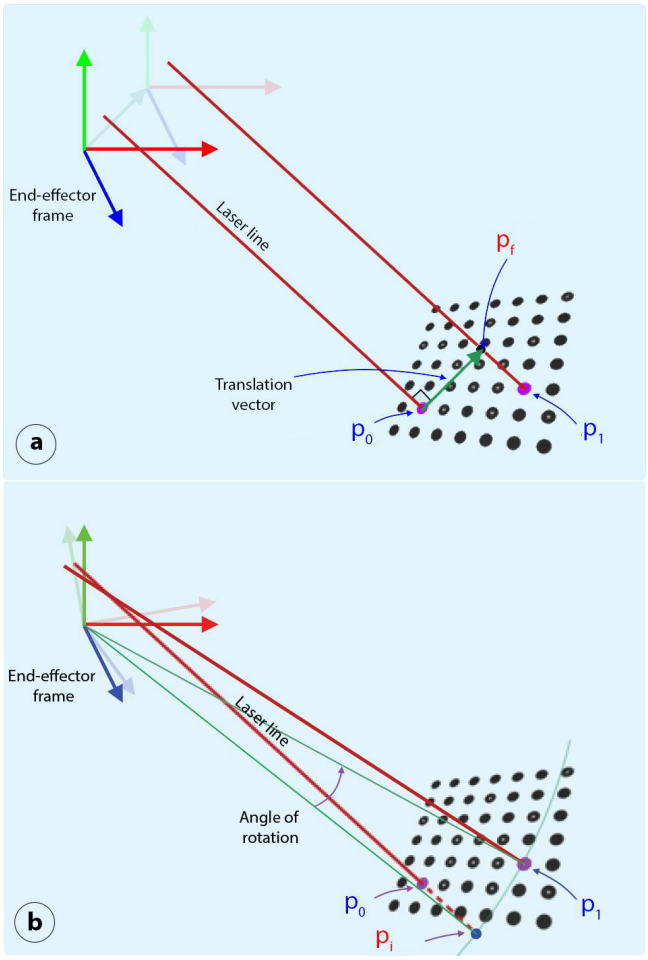

Figure 11: (a) Calculation method of the pure translation motion. (b) Calculation method of the pure rotation motion.

The obtained results are shown in (Fig.12), where 9 points have been chosen to

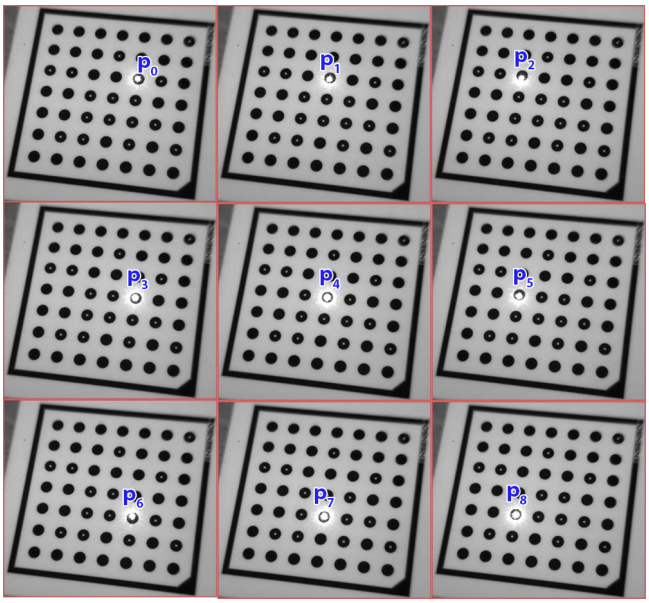

Figure 12: Validation method results: targeting 9 arbitrary points with two types of end-effector motion, pure rotation and pure translation.

be targeted with the two types of end-effector motion presented previously. The Laser is initially targeting point $\mathbf{p_0}$. The experiments show that the Laser points correctly the chosen 9 points with very small error. Table 2 shows the targeting error both in the image plane (pixel) and in the space (μm) for each of the 9 points. The average targeting error is 322.04μm.

5.2. Magnetic microrobot guiding using the vision-based platform

The aim of this experimental part is to highlight the existence of the convergence point and to show the feasibility of microrobot steering using the proposed platform in both open-loop and closed schemes. As it is shown on Fig.1, the used prototyping platform is composed by a magnetic actuator, camera and two microscopes (hybrid vision system), and robot manipulator to perform the positioning of the actuator. The workspace where the microrobot evolve has a circular shape (Fig.13) filled with viscous liquid composed of a mixture of 80% water and 20% glycerol with a dynamic viscosity of $17.288\times10^{-4}\ Ns/m^2$. The used microrobot in the experiments is approximately of

Table 2: Results of the validation method for the chosen 9 points.

Points	Targeting error in image	Targeting error in space
Point 0	5.83 pixel	489.3μm
Point 1	5.38 pixel	430.8μm
Point 2	7.61 pixel	491.7μm
Point 3	3.60 pixel	288.8μm
Point 4	1.41 pixel	188.5μm
Point 5	3.00 pixel	199.8μm
Point 6	5.00 pixel	405.8μm
Point 7	3.16 pixel	237.2μm
Point 8	1.41 pixel	166.5μm

spherical form with a radius around 250μm.

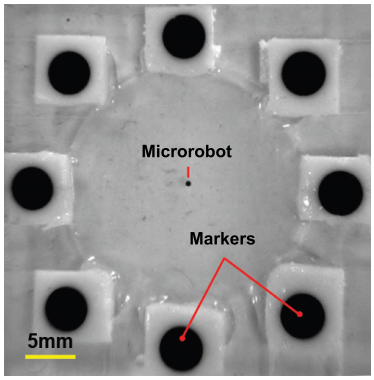

Figure 13: The workspace were the microrobot is controlled. The markers placed on the workspace are used by the vision system to detect its movement.

5.2.1. Validation of the existence of convergence point and open loop perturbation compensation in a planar workspace

The magnetic actuator has been positioned adequately such that the convergence point is in the middle of the micro-workspace (refer to Fig. 15.(a)). This facilitates

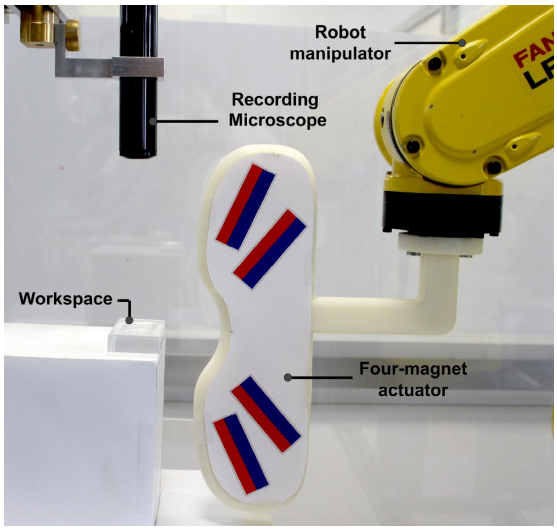

Figure 14: Experimental setup: the robot manipulator to position the actuator. The microscope, to only visualize the particle in the workspace, and the workspace is a rectangular shape with dimensions of 2x3cm where the particle is placed.

highlighting the convergence point existence and effect. Its position expressed in the end effector frame has been recovered using the hybrid vision system as explained in section 4 and the obtained numerical value is equal to ${}^{eff}\mathbf{x}_{cp} = \begin{bmatrix} 8.78 & 7.11 & -8.83 \end{bmatrix}^T cm$. To demonstrate the effect of the local maximum, a small permanent magnet is brought close to the workspace to shift the particle from its stable position to another. Then, the particle is released by moving away the small magnet from the workspace. The trajectories followed by the micro-particles from the different initial positions are shown in Fig.15. As predicted, the particle returns to its stable position, which is the correspond local maxima of the magnetic field magnitude generated by the actuator. The obtained results also show that particle returns to the local maximum following path inflected the actuator force vectors. Actually, the force map projected on the workspace as shown on Fig.15 have been obtained based on the actuator model.

The previous experimental results have shown that the actuator is capable of converging a microrobot to a specific point in a plane. In the new set of experiment this ability is tested while the particles have to be moved along a well defined trajectory in

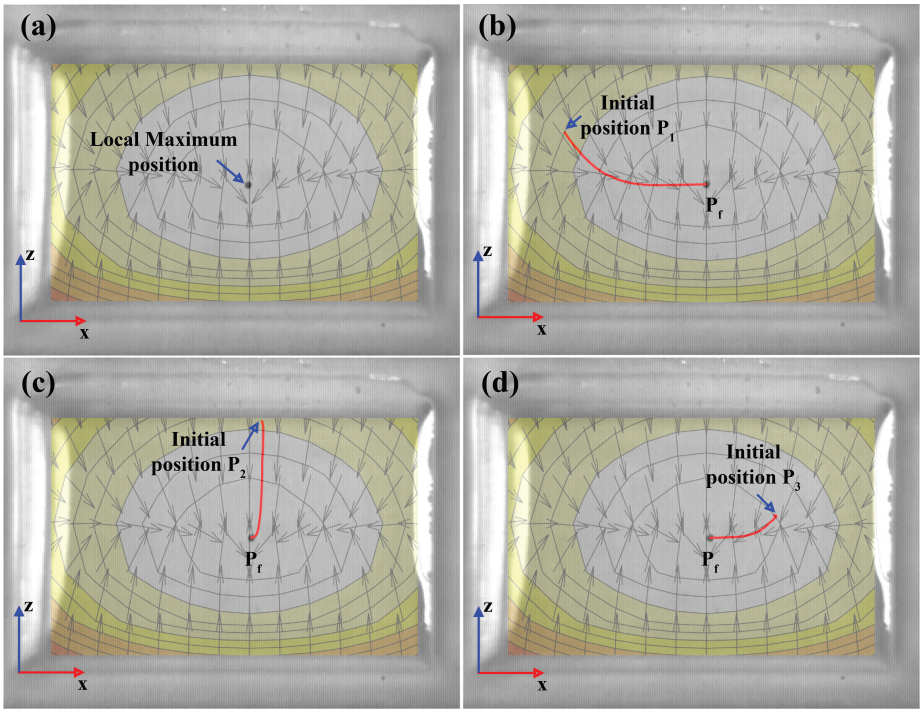

Figure 15: Convergence point validation results: (a) shows the magnetic particle initial position at a local maximum, (b), (c) and (d) are the particle trajectories when moving back from positions 1, 2 and 3 respectively, to its initial position under the action of magnetic force. The simulation results of the magnetic force direction are printed in the background of the workspace.

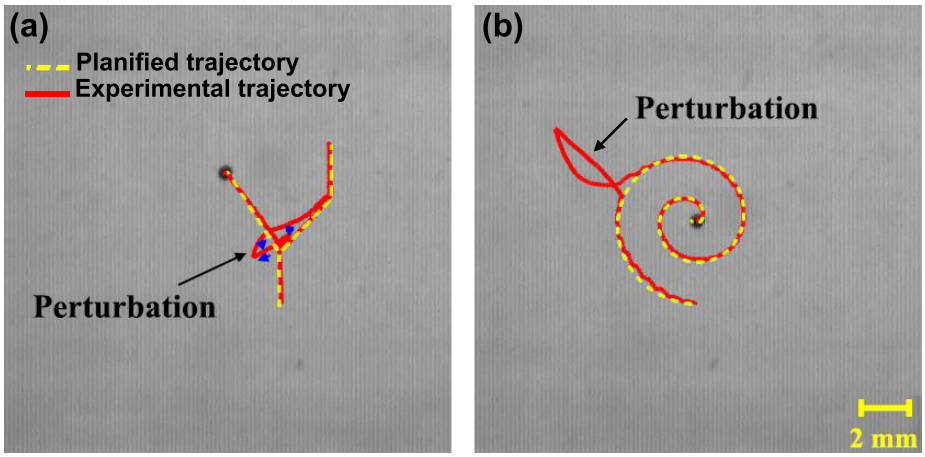

Figure 16: The pictures present the trajectory tracking results between the predefined and the experimental trajectory, respectively: (a) for a segmented linear trajectory, and (b) for a spiral trajectory.

an open loop. Two types of trajectories have been considered: trajectory composed of linear segments, and a spiral. For each trajectory, the actuator is moved to its initial position ensuring that the convergence point and the first point of the trajectory coincide. As the convergence area covers all the rectangular workspace, whatever the initial position of the particle, its convergence to the starting point is ensured. This capacity is important and could be critical when guiding microrobots inside the human body. Actually, based on this property, moving the convergence point along the predefined trajectory makes the particle follow the same path. Figures (Fig. 16 (a) and (b)) show the obtained results for the two considered trajectories tracking with the presence of perturbations introduced by bringing a small permanent magnet close to the particle workspace. The obtained plots show the ability of the proposed actuator to achieve magnetic microrobot with an open loop control scheme.

5.2.2. Vision-based actuator positioning, perturbation compensation and microrobot steering strategy

The first set of experiments considered trajectory following by a microrobot in static micro workspace.The particles are driven by positioning the actuator using the pose of its rigidly attached pattern with respect to the camera. The following experi-

ment considers scenarios of moving micro-workspace. For instance, this can happen in the case of targeted drug delivery a moving internal ear due the patients head movement. Actually, as it is the case for other medical applications, optical trackers fixed on the patient's head can be used to recover this kind of movements. Here, two options are possibles to follow the workspace, either with the camera by attaching markers that are visible by the camera to the workspace. Alternatively, with microscopes by gluing small markers directly onto the workspace. Choosing the second option, two type trajectory types have been released, rectangular and spiral trajectory. Those trajectories have been first defined in coordinates system related to the microscopes, then expressed in the robot end-effector frame taking into account the movements of the micro-workspace. The obtained results of trajectory following are shown in Fig.17 (a) and Fig.17(b), at a moment during the navigation, disturbances are simulated by moving the workspace to assess the trajectory correction using the vision system.Fig.17 (c) and Fig.17(d) show the norm of the error between the predefined and the experimental trajectory. ; the error is calculated from start to end point of the trajectory. From the plots, it can be seen that initially, the particle follows the desired trajectory with error less than $100\mu m$ for the rectangular trajectory and less than $400\mu m$ for the spiral trajectory. At the moment of disturbance at 25^{th} point for the rectangular trajectory and 90^{th}point for the spiral trajectory, we observe the peaks that represent the maximal error before adjusting the actuator position with respect to the new workspace position. After adjusting the actuator position, the error is minimized and the particle has come back to follow the desired trajectory.

The second experiment of this part aims to explore the possibility of using visual feedback on the position of the microrobot when it is accessible. Such scenario can be considered for the case of the eye where its interior can be seen with a vision system. On the contrary of the open-loop scheme, in the closed-loop control the time needed to follow a trajectory is reduced, because it is no longer needed to calculate the maximum time needed to move the microrobot from one point to another. The obtained results of this experiment are shown in Fig.18, where a complex trajectory has been considered. In the closed loop, a standard error of $200\mu m$ has been tolerated to move to the next point of the trajectory, that's why a small gap is noticed in some points of

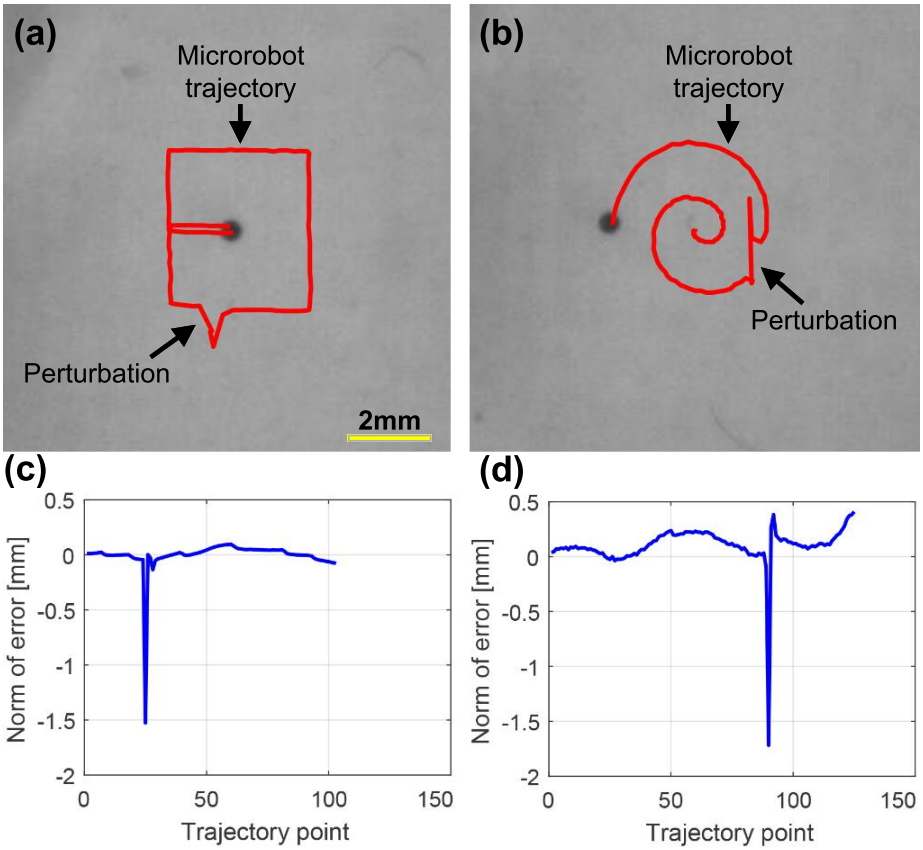

Figure 17: The pictures present the results of the open-loop trajectory tracking and closed-loop workspace position correction, and the error results between the predefined and the experimental trajectory, respectively: (a) and (c) for a rectangular trajectory , (b) and (d) for a spiral trajectory.

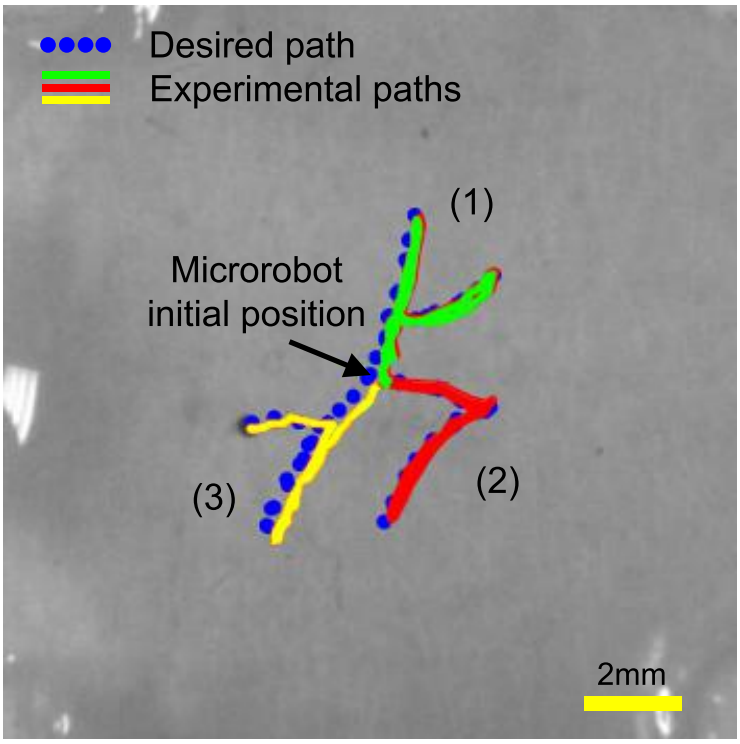

Figure 18: Results of the closed-loop trajectory tracking experiment. (1), (2) and (3) are three trajectories released with same initial point

the trajectories.

5.2.3. Microrobot navigation in presence of obstacle

The experiment aims to study the effect of obstacles in the microrobot workspace. The experiment consists in making the microrobot crosses an obstacle formed by "wall of the bristles", while following a linear trajectory back and forth. The goal is to visualize how the microrobt will cross the wall of the bristles. The results of this experiment are shown in Fig.19 (b), (c), (d), (e) and (f) where the particle initially performs a linear trajectory as desired. Once the particle reaches the obstacles, the magnetic force forces the particle to cross the wall of bristles with a small deviation. Once the obstacle is crossed, the particle joins its planned trajectory (see Fig.19 (c)). The influence on the horizontal navigation due to changes in vertical direction depends

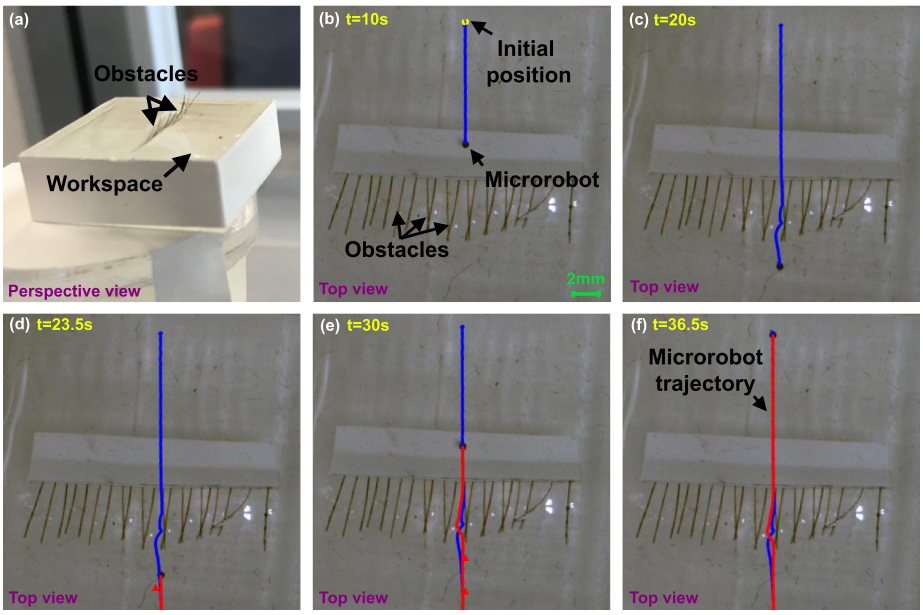

Figure 19: Results of the microrobot navigation experiment in the presence of obstacles. (a) The perspective view of the bristles obstacle. (b), (c), (d), (e) and (f) are the top view of different steps of the round trip trajectory of the micrororobot released in presence obstacle.

on the magnetic force generated by the actuator. If the magnetic force is strong enough, the actuator will push a microrobot in ragged or arcuate surface. Otherwise, if the magnetic force is not strong enough, a ragged surface will result in friction that may stop up the robot displacements.

6. Conclusion

This paper proposed a solution for precise magnetic microrobot trajectory tracking which is a vision-based magnetic platform. The two main components of the platform are permanent magnets based actuator and a hybrid vision system. The magnetic actuator is a four-magnet based actuator capable of generating a convergence point at a distance in the plane, which facilitates the control of microrobots. Its design principle and method to create the local maxima of magnetic field magnitude at a distance are explained. The hybrid vision system is composed by camera and two microscopes used mainly to create a link between a micro scale environment where the microrobots are

guided and the macro scale where the magnetic actuator is controlled. This allows to study the dynamics of microrobots in viscous environment and to estimate precisely the convergence point position with respect to end-effector. Microrobots steering strategy is proposed to demonstrate the feasibility of the robotic platform to control the microrobot in both closed environments and others that are accessible for visual feedback. The platform main components and the steering strategy are validated experimentally. The results of the proposed calibration method before and after refinement are presented. The existence of convergence point generated by the actuator is demonstrated. Two experiments using open-loop and closed-loop schemes are carried out to validate the steering strategy using the proposed platform. Future work will be devoted to improving the current actuator by optimizing its structure.

Acknowledgments

This work was supported by the CochléRob project funded by Région Centre, HEI campus Centre, and Châteauroux Métropole.

References

[1] H. Tillander, Magnetic guidance of a catheter with articulated steel tip, Acta Radiologica 35 (1) (1951) 62–64.

[2] M. Equen, G. ROACH, R. BROWN, T. Bennett, Magnetic removal of foreign bodies from the esophagus, stomach, and duodenum, AMA archives of otolaryngology 66 (6) (1957) 698–706.

[3] G. Gillies, R. Ritter, W. Broaddus, M. Grady, M. Howard III, R. McNeil, Magnetic manipulation instrumentation for medical physics research, Review of Scientific Instruments 65 (3) (1994) 533–562.

[4] A. Chiba, Moving of a magnetic actuator for a capsule endoscope in the intestine of a pig, J. Magn. Soc. Jpn. 29 (2005) 343–346.

[5] E. Morita, N. Ohtsuka, Y. Shindo, S. Nouda, T. Kuramoto, T. Inoue, M. Murano, E. Umegaki, K. Higuchi, In vivo trial of a driving system for a self-propelling capsule endoscope using a magnetic field (with video), Gastrointestinal endoscopy 72 (4) (2010) 836–840.

[6] G. Kósa, P. Jakab, F. Jólesz, N. Hata, Swimming capsule endoscope using static and rf magnetic field of mri for propulsion, in: Robotics and Automation, 2008. ICRA 2008. IEEE International Conference on, IEEE, 2008, pp. 2922–2927.

[7] D. Montgomery, R. Weggel, M. Leupold, S. Yodh, R. Wright, Superconducting magnet system for intravascular navigation, Journal of Applied Physics 40 (5) (1969) 2129–2132.

[8] A. W. Mahoney, J. J. Abbott, 5-dof manipulation of an untethered magnetic device in fluid using a single permanent magnet, Proc Robot Sci Syst (2014) 1–19.

[9] A. W. Mahoney, J. J. Abbott, Generating rotating magnetic fields with a single permanent magnet for propulsion of untethered magnetic devices in a lumen, IEEE Transactions on Robotics 30 (2) (2014) 411–420.

[10] M. Simi, P. Valdastri, C. Quaglia, A. Menciassi, P. Dario, Design, fabrication, and testing of a capsule with hybrid locomotion for gastrointestinal tract exploration, IEEe/ASME Transactions on Mechatronics 15 (2) (2010) 170–180.

[11] P. Valdastri, C. Quaglia, E. Buselli, A. Arezzo, N. Di Lorenzo, M. Morino, A. Menciassi, P. Dario, A magnetic internal mechanism for precise orientation of the camera in wireless endoluminal applications, Endoscopy 42 (06) (2010) 481–486.

[12] P. Valdastri, E. Sinibaldi, S. Caccavaro, G. Tortora, A. Menciassi, P. Dario, A novel magnetic actuation system for miniature swimming robots, IEEE Transactions on Robotics 27 (4) (2011) 769–779.

[13] G. Ciuti, R. Donlin, P. Valdastri, A. Arezzo, A. Menciassi, M. Morino, P. Dario, Robotic versus manual control in magnetic steering of an endoscopic capsule, Endoscopy 42 (02) (2010) 148–152.

[14] F. Carpi, C. Pappone, Stereotaxis niobe® magnetic navigation system for endocardial catheter ablation and gastrointestinal capsule endoscopy, Expert review of medical devices 6 (5) (2009) 487–498.

[15] P. Lébraly, E. Royer, O. Ait-Aider, C. Deymier, M. Dhome, Fast calibration of embedded non-overlapping cameras, in: Robotics and Automation (ICRA), 2011 IEEE International Conference on, 2011, pp. 221–227. doi:10.1109/ICRA.2011.5979743.

[16] R. K. Kumar, A. Ilie, J. M. Frahm, M. Pollefeys, Simple calibration of non-overlapping cameras with a mirror, in: Computer Vision and Pattern Recognition, 2008. CVPR 2008. IEEE Conference on, 2008, pp. 1–7. doi:10.1109/CVPR.2008.4587676.

[17] R. Ravaud, G. Lemarquand, Magnetic field produced by a parallelepipedic magnet of various and uniform polarization, Progress In Electromagnetics Research 98 (2009) 207–219.

[18] J. J. Moré, The levenberg-marquardt algorithm: implementation and theory, in: Numerical analysis, Springer, 1978, pp. 105–116.

[19] R. K. Lenz, R. Y. Tsai, Calibrating a cartesian robot with eye-on-hand configuration independent of eye-to-hand relationship, IEEE transactions on pattern analysis and machine intelligence 11 (9) (1989) 916–928.

[20] S. Wijesoma, D. Wolfe, R. Richards, Eye-to-hand coordination for vision-guided robot control applications, The International Journal of Robotics Research 12 (1) (1993) 65–78.

[21] K. Belharet, D. Folio, A. Ferreira, Control of a magnetic microrobot navigating in microfluidic arterial bifurcations through pulsatile and viscous flow, in: Intelligent Robots and Systems (IROS), 2012 IEEE/RSJ International Conference on, IEEE, 2012, pp. 2559–2564.

[22] Q. A. Pankhurst, J. Connolly, S. K. Jones, J. Dobson, Applications of magnetic nanoparticles in biomedicine, Journal of physics D: Applied physics 36 (13) (2003) R167.

[23] K. Belharet, D. Folio, A. Ferreira, Endovascular navigation of a ferromagnetic microrobot using mri-based predictive control, in: Intelligent Robots and Systems (IROS), 2010 IEEE/RSJ International Conference on, IEEE, 2010, pp. 2804–2809.

[24] Y. Okuhata, Delivery of diagnostic agents for magnetic resonance imaging, Advanced drug delivery reviews 37 (1) (1999) 121–137.